MNRAS Advance Access published May 23, 2016

Herschel protocluster survey: A search for dusty star-forming galaxies in protoclusters at $z = 2 - 3$

Y. Kato,[1,2⋆] Y. Matsuda,[1,3] Ian Smail,[4,5] A. M. Swinbank,[4,5] B. Hatsukade,[1] H. Umehata,[6,7] I. Tanaka,[8] T. Saito,[1] D. Iono,[1,3] Y. Tamura,[7] K. Kohno,[7,9] D. K. Erb,[10] B. D. Lehmer,[11] J. E. Geach,[12] C. C. Steidel,[13] D. M. Alexander,[4] T. Yamada[14] and T. Hayashino[15]

[1] *National Astronomical Observatory of Japan, 2-21-1 Osawa, Mitaka, Tokyo, 181-8588, Japan*
[2] *Department of Astronomy, Graduate school of Science, The University of Tokyo, 7-3-1 Hongo, Bunkyo-ku, Tokyo 133-0033, Japan*
[3] *Department of Astronomy, School of Science, The Graduate University for Advanced Studies (SOKENDAI), Osawa, Mitaka, Tokyo 181-8588, Japan*
[4] *Centre for Extragalactic Astronomy, Department of Physics, Durham University, South Road, Durham, DH1 3LE, UK*
[5] *Institute for Computational Cosmology, Durham University, South Road, Durham DH1 3LE, UK*
[6] *European Southern Observatory, Karl-Schwarzschild-Str. 2, D-85748 Garching, Germany*
[7] *Institute of Astronomy, School of Science, The University of Tokyo, 2-21-1 Osawa, Mitaka, Tokyo 181-0015, Japan*
[8] *Subaru Telescope, National Astronomical Observatory of Japan, 650 North AâĂŹohoku Place, Hilo, HI 96720, USA*
[9] *Research Center for the Early Universe, The University of Tokyo, 7-3-1 Hongo, Bunkyo, Tokyo 113-0033*
[10] *Center for Gravitation, Cosmology and Astrophysics, Department of Physics, University of Wisconsin Milwaukee 3135 North Maryland Avenue, Milwaukee, Wisconsin 53211, USA*
[11] *Department of Physics, University of Arkansas, 226 Physics Building, 835 West Dickson Street, Fayetteville, AR 72701, USA*
[12] *Centre for Astrophysics Research, Science & Technology Research Institute, University of Hertfordshire, Hatfield, AL10 9AB, UK*
[13] *California Institute of Technology, MS 249-17, Pasadena, CA 91125, USA*
[14] *Institute of Space Astronautical Science, Japan Aerospace Exploration Agency, Sagamihara, Kanagawa 252-5210, Japan*
[15] *Research Center for Neutrino Science, Tohoku University, Sendai, Miyagi, 980-8578, Japan*

23 May 2016

ABSTRACT

We present a *Herschel*/SPIRE survey of three protoclusters at $z = 2 - 3$ (2QZCluster, HS1700, SSA22). Based on the SPIRE colours (S_{350}/S_{250} and S_{500}/S_{350}) of 250 μm sources, we selected high redshift dusty star-forming galaxies potentially associated with the protoclusters. In the 2QZCluster field, we found a 4σ overdensity of six SPIRE sources around $4.5'$ (~ 2.2 Mpc) from a density peak of Hα emitters at $z = 2.2$. In the HS1700 field, we found a 5σ overdensity of eight SPIRE sources around $2.1'$ (~ 1.0 Mpc) from a density peak of LBGs at $z = 2.3$. We did not find any significant overdensities in SSA22 field, but we found three 500 μm sources are concentrated $3'$ ($\sim$1.4 Mpc) east to the LAEs overdensity. If all the SPIRE sources in these three overdensities are associated with protoclusters, the inferred star-formation rate densities are $10^3 - 10^4$ times higher than the average value at the same redshifts. This suggests that dusty star-formation activity could be very strongly enhanced in $z \sim 2 - 3$ protoclusters. Further observations are needed to confirm the redshifts of the SPIRE sources and to investigate what processes enhance the dusty star-formation activity in $z \sim 2 - 3$ protoclusters.

Key words: galaxies: clusters: individual – galaxies: individual – galaxies: formation – galaxies: high-redshift – submillimetre: galaxies – infrared: galaxies

1 INTRODUCTION

The central regions of local clusters are dominated by passive early-type ellipticals and spheroidals, their stellar populations are old, with inferred formation redshifts of $z \gtrsim 2$ (e.g., Ellis et al. 1997). High-redshift dusty star-forming galaxies (DSFGs) are strongly star-forming galaxies (SFR $\gtrsim 100 - 1000$ M$_\odot$ yr^{-1}) and have been proposed to the precursors of present-day ellipticals in local clusters (e.g., Lilly et al. 1998; Smail et al. 1998; Lutz et al. 2001; Ivison et al. 2013). Large hydro-dynamical simulations and galaxy formation models predict intense star formation could be detectable as concentrations of DSFGs in $z \gtrsim 2$ protoclusters (e.g., Granato et al. 2015). Indeed, there have been reports of a reversal of the SFR-density relation (e.g., Elbaz et al. 2007;

⋆ E-mail:kato.yu@nao.ac.jp

Tran et al. 2010), which is increasing SFR with increasing local density at $z \gtrsim 1$. Protoclusters at $z \gtrsim 2$ are thus unique laboratories to explore bursting star-formation in a critical epoch of galaxy formation (Casey 2016).

A numbers of studies have confirmed the presence of DSFGs in $z < 2$ galaxy clusters (e.g., Brodwin et al. 2013; Smail et al. 2014; Ma et al. 2015; Webb et al. 2015), while studies confirming DSFGs at $z \gtrsim 2$ protoclusters are also progressing (e.g., Tamura et al. 2009; Clements et al. 2014; Umehata et al. 2014, 2015; Casey et al. 2015). Some surveys to search for DSFGs at far-infrared wavelengths have focused on radio galaxy fields (e.g., Stevens et al. 2003; Valtchanov et al. 2013; Rigby et al. 2014; Dannerbauer et al. 2014). Radio galaxies are thought to be tracers of large scale structures, and some fraction of $z \gtrsim 2$ protoclusters around radio galaxies indeed appear to have experienced bursting dusty star-formation related to DSFGs (e.g., Ivison et al. 2000). However, such regions may be biased by the end to host a currently accreting Super Massive Black Hole (SMBH) and so we also need to explore DSFGs large-scale structures selected by other techniques at $z \gtrsim 2$ to investigate bursting star-formation more generally. Clements et al. (2014) investigated ~ 90 deg^2 sky observed as part of the HerMES survey with *Planck* and *Herschel* to search for clusters undergoing dusty star-formation. They found four candidate clusters, and for all four cases they found evidence of galaxy clusters with red-sequence based on optical/NIR data. The star-formation rate density of these at $z \gtrsim 2$ are four order of magnitudes higher than the cosmic averaged values. But is this also true for dusty star-formation in known optical/UV-selected galaxy clusters at $z \gtrsim 2$?

In this paper, we report a result of observations with the Spectral and Photometric Imaging Receiver (SPIRE; Griffin et al. 2010) on the *Herschel Space Observatory* (*HSO*; Pilbratt et al. 2010) for three protoclusters at $z = 2-3$ (2QZCluster, HS1700, and SSA22 at $z = 2.2$, 2.3, and 3.1, respectively). The three protoclusters have filamentary, large scale structures of rest-frame UV to optical selected galaxies. The structure of this paper is following. In §2 we introduce the *Herschel*/SPIRE observations, the data processing, and our targeted fields. In §3 we present source detection methods, number counts, and SPIRE colour selection. In §4 and §5 we present our results, discussion, and then summarize our main findings. We use the following cosmological parameters: $\Omega_m = 0.3$, $\Omega_\Lambda = 0.7$, $h = 0.7$. In this cosmology, the Universe is 2.9, 2.8, and 2.0 Gyr old and $1.0''$ corresponds to 8.3, 8.2 and 7.6 kpc in physical length at $z = 2.2$, 2.3 and 3.1, respectively.

2 OBSERVATIONS & TARGET FIELDS

2.1 SPIRE OBSERVATIONS

Our *Herschel*/SPIRE observations were performed as part of the second Open Time (OT2) *Herschel* programs (PI: Y. Matsuda). We summarize the observations in Table 1. The observations were executed in Large Map mode with a scan rate of $30''$ s^{-1}, repeated 14 times for each field ($N_{\rm rep}$=14). The dates of observations are 22 June 2012 (2QZCluster), 4 March 2012 (HS1700), and 10 May 2012 (SSA22). The coverage of the maps are $\sim 23' \times 23'$ (2QZCluster), $\sim 22' \times 22'$ (HS1700), and $\sim 33' \times 33'$ (SSA22) corresponding to $\sim 40-60$ comoving Mpc at the protocluster redshifts, which are sufficient to search for concentration of DSFGs around the density peak of protocluster members. The integration times are 1.8, 1.5 and 3.7 hours for 2QZCluster, HS1700 and SSA22, respectively. Maps were produced with the *Herschel* Interactive Processing Environment (HIPE, v11.0.0), following the standard data processing and map-making steps with destriping. The full width at half maximum (FWHM) of the SPIRE beam is $18.1''$, $24.9''$ and $36.6''$ at 250, 350 and 500 μm, respectively (Swinyard et al. 2010). The final maps have pixel sizes of $6''$, $10''$, and $14''$ at 250, 350, and 500 μm. We measured the 1σ confusion noise ($\sigma_{\rm conf}$) as map variance of flux density within effective area (Table 1), which are slightly higher than the values of blank fields (Nguyen et al. 2010). The instrumental noise measured in our three protoclusters are about one-third of the confusion noise (Table 1).

2.2 PROTOCLUSTER TARGETS

2QZCluster; This protocluster was originally identified as a concentration of five Quasi Stellar Objects (QSOs) in a ~ 1 degree region at $z = 2.23$ from the 2dF Quasar Redshift survey (Croom et al. 2001, 2004). Four out of the five QSOs are even more strongly clustered in a 30×30 comoving Mpc patch. An Hα narrow-band imaging revealed a filamentary large-scale structure of an over density of 22 HAEs connecting the QSOs (Matsuda et al. 2011). *Chandra*/ACIS-I 100 ks observations of this structure also showed evidence that the Active Galactic Nucleus (AGNs) fraction is a factor of ~ 3.5 higher than blank fields (Lehmer et al. 2013).

HS1700; This protocluster was originally discovered as a $\sim 7\times$ density contrast redshift spike of UV/optical-selected star forming galaxies (BX/BM) within a ~ 25 comoving Mpc region at $z = 2.30$ (Steidel et al. 2005). A Lyα narrowband imaging survey revealed a filamentary large-scale structure of six giant Lyα Blobs (LABs) (Erb, Bogosavljević, & Steidel 2011). *Chandra*/ACIS-I 200 ks observations of this structure also showed tentative evidence of an enhancement of AGN fraction compared to the field environment (Digby-North et al. 2010).

SSA22; This protocluster was originally discovered as a $\sim 4-6\times$ density contrast in redshift distribution of Lyman Break Galaxies (LBGs) and Lyα emitters (LAEs) within a ~ 20 comoving Mpc region at $z = 3.09$ (Steidel et al. 1998, 2000). A wide-field Lyα narrowband imaging survey with Subaru Telescope revealed a filamentary large-scale structure of 283 LAEs, extended to at least ~ 60 comoving Mpc (Hayashino et al. 2004). This sample of LAEs includes 35 LABs with sizes of 30–150 kpc scale (Steidel et al. 2000; Matsuda et al. 2004). *Chandra*/ACIS-I 400 ks observations of this structure showed that the AGN fraction of protocluster members is $\sim 3\times$ higher than that in the field environment (Lehmer et al. 2009a,b).

Blank field (COSMOS); We have chosen well-studied extragalactic field Cosmic Evolution Survey (COSMOS) to use as a blank field, which is observed as a part of *Herschel* Multi-tiered Extra-galactic survey, HerMES (Oliver et al. 2012). The SPIRE map in COSMOS field is larger and deeper than our observations, so we have reprocessed them by limiting to the same depth using $N_{\rm rep} = 14$. Subse-

Table 1. Summary of our *Herschel*/SPIRE observations.

Target	z^a	R.A.^{b}	Dec^c	Area^d	$t_{\rm int}{}^e$	$\sigma_{\rm conf}{}^f$			$\sigma_{\rm inst}{}^g$		
						S_{250}	S_{350}	S_{500}	S_{250}	S_{350}	S_{500}
		(J2000)	(J2000)	(arcmin^2)	(hours)	(mJy)	(mJy)	(mJy)	(mJy)	(mJy)	(mJy)
2QZCluster	2.230 ± 0.016	10h03m51s	+00d15m09s	515	1.8	6.7	7.0	7.1	2.0–3.9	1.6–2.6	2.0–3.3
HS1700	2.300 ± 0.015	17h01m15s	+64d14m03s	497	1.5	7.3	7.4	7.5	2.0–3.7	1.6–2.7	2.0–3.2
SSA22	3.09 ± 0.03	22h17m34s	+00d17m01s	1076	3.7	7.7	7.8	8.0	1.9–3.2	1.6–2.4	1.9–3.0
COSMOS	-	10h00m37s	+02d11m26s	3422	50.1	7.1	7.7	7.8	2.1–2.7	1.7–2.0	2.1–2.8

Notes. (a): Redshift range of the member galaxies, based on HAEs for 2QZCluster (Matsuda et al. 2011) and LBGs for HS1700 (Steidel et al. 2005) and SSA22 (Steidel et al. 1998, 2000). (b), (c): The coordinates of the field centre of *Herschel*/SPIRE observations. (d): The area where the integration time is greater than 30%. For COSMOS field, we used centre of 3422 arcmin^2 area. We detected sources within this area. (see also Figure 3). (e): The total integration time. For the survey design of COSMOS field, please see Oliver et al. (2012). (f), (g): The confusion noise and instrumental noise.

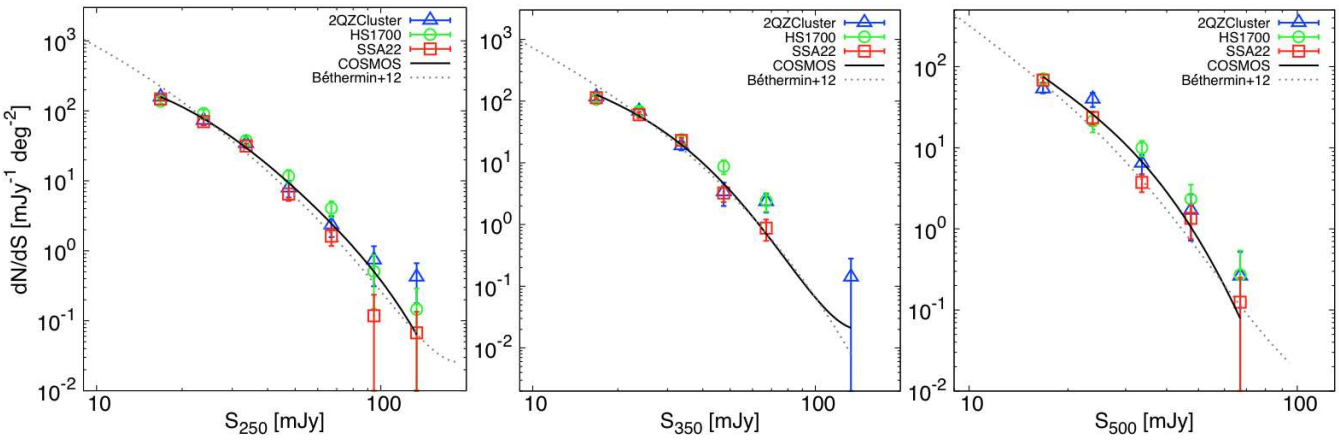

Figure 1. Number counts at 250, 350 and 500 μm in the three protoclusters and COSMOS field. We detected S/N $>$ 2 sources in the 250 μm maps and measured the 350 and 500 μm fluxes at the positions of the 250 μm sources. We fitted the data points of COSMOS filed with a bézier curve. The number counts of the SPIRE sources in the protoclusters averaged over their full fields are roughly consistent with those of COSMOS field. The number counts of the SPIRE sources in COSMOS field are also consistent with those of HerMES blank fields (Béthermin et al. 2012), suggesting that COSMOS field can be used as a control field.

quently, we apply the same map making, and source detection procedure in order to make sure that we match the depth of our observations. The confusion and instrumental noise values are given in Table 1.

3 ANALYSIS

3.1 DETECTION & NUMBER COUNTS

The source detection was conducted on the 250 μm maps, because of the better spatial resolution compared with longer wavelength bands. We cation that 500 μm detection causes a source blending (even 250 μm can deblend these) and large spatial uncertainty. We used the SUSSEXTRACTOR (Smith et al. 2012) for the source detection and photometry. We detected S/N $>$ 2 sources in the maps within the region where the integration time is greater than 30% of the deepest parts (515 arcmin^2 for 2QZCluster, 497 arcmin^2 for HS1700, 1076 arcmin^2 for SSA22, and 3422 arcmin^2 for COSMOS field). We measured 350 μm and 500 μm fluxes at the positions of sources detected in the 250 μm maps, then listed these 250 μm sources only if the flux density is above 12 mJy in at least one of the SPIRE bands (See also Table 8–10, and the full tables are avaivable in online). This flux density limit corresponds to $\sim 4\sigma$ of the instrumental noise and $\sim 2\sigma$ of the confusion noise in all three bands. For SSA22, we cut out the region shown in Figure 3 due to the high background fluxes from the Galactic cirrus.

We compared these SPIRE number counts with COSMOS field. We show the raw (i.e., not corrected for the completeness) number counts in Figure 1 (See also Table 5– 7). The raw number counts are roughly consistent with COSMOS field data at $>$ 20 mJy bin at 250 and 350 μm. A moderate excess of number counts at $S_{350} > 50$ mJy and $S_{500} > 40$ mJy were found (by a factor of 2–3) in HS1700 and 2QZCluster, although they are within the error bars based on Poisson noise. We also compared number counts in COSMOS field with wider HerMES survey data (Béthermin et al. 2012). The number counts in COSMOS field agree with that of HerMES survey data, suggesting that COSMOS field is suitable as a control field.

Table 2. Summary of *Herschel*/SPIRE sources in the three protoclusters.

Field	Area[a] (arcmin^{-2})	N[b] (prior)	N[c] (catalogued)	N[d] (selected)	N[e]	Σ^f (arcmin^{-2})	Σ^g (arcmin^{-2})	δ^h	σ^i
2QZCluster	515	643	399	12	6	0.023 ± 0.007	0.132 ± 0.054	3.0 ± 1.7	3.9 ± 2.1
HS1700	497	579	383	26	8	0.052 ± 0.010	0.186 ± 0.066	3.7 ± 1.7	5.0 ± 2.2
SSA22	1076	1253	772	55	5	0.051 ± 0.007	-	-	-
COSMOS (matched to 2QZCluster)	3422	4923	2777	111	7	0.032 ± 0.003	-	-	-
COSMOS (matched to HS1700)	3422	4923	2777	140	7	0.041 ± 0.004	-	-	-
COSMOS (matched to SSA22)	3422	4923	2777	262	10	0.077 ± 0.005	-	-	-

Notes. (a): The area where the integration time is greater than 30%. We detected sources within this area. (b): The numbers of S/N (250 μm) > 2 prior sources. (c): The numbers of catalogued sources which at least one SPIRE band flux is above 12 mJy. (d): The numbers of colour-selected bright SPIRE sources. For SSA22, we excluded the sources in high background fluxes (see Figure 3). (e): The numbers of colour-selected bright SPIRE sources within the overdensities. (f): The surface density of colour-selected bright SPIRE sources. The errors assume Poisson statistics. (g): The surface density of colour-selected bright SPIRE sources in the overdensities, assume an area of the overdensities ($r = 3.8'$ for 2QZCluster, $r = 3.7'$ for HS1700). The errors assume Poisson statistics. (h) − (i): The δ and σ are calculated from $\delta_{\rm pc} = (n_{\rm pc} - n_{\rm ave})/n_{\rm ave}$ and $\sigma_{\rm pc} = (n_{\rm pc} - n_{\rm ave})/\sigma_{\rm ave}$. The errors assume Poisson statistics.

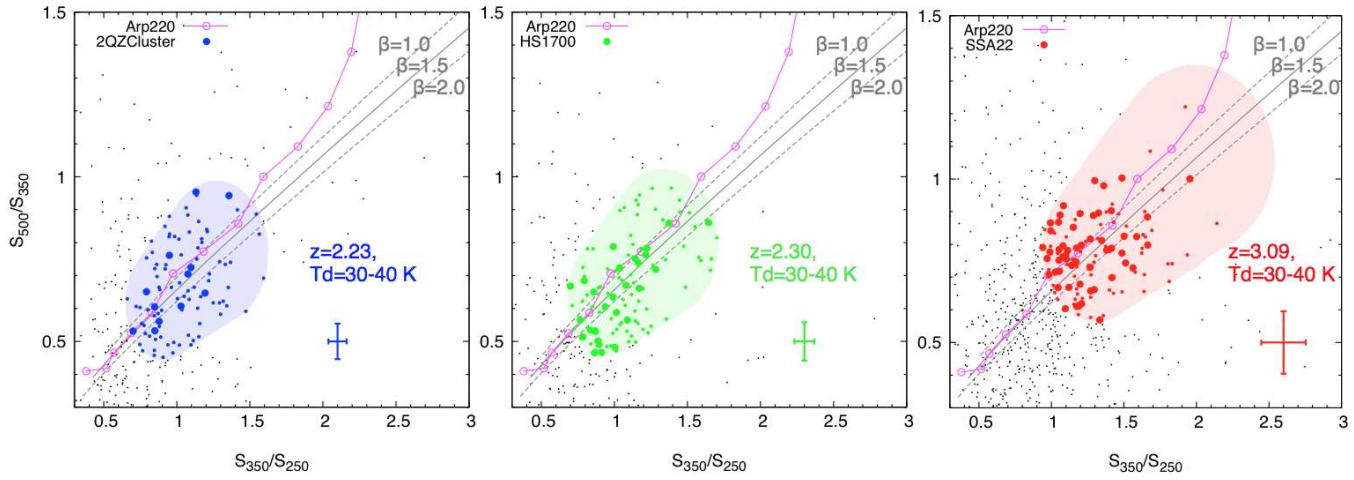

Figure 2. S_{500}/S_{350} vs S_{350}/S_{250} colour-colour diagram of the 250 μm sources. From left to right, we show the plots for 2QZCluster, HS1700, and SSA22. We selected candidates of DSFGs possibly associated with the protoclusters whose colours are consistent with a single gray body SEDs including a photometric error of ± 20% (shaded regions). We assume the protocluster redshifts, dust temperatures of $T_d = 30 - 40$ K and dust emissivity $\beta = 1.5$. The grey solid and dashed lines show tracks of single grey body SEDs for different β. We plot sources with fluxes above 12mJy in least one SPIRE bands as small grey points. The coloured larger/smaller symbols show sources with $L_{\rm FIR}$ larger/smaller than 5.0×10^{12} $L_\odot$. The error bars show the average errors of colour-selected bright SPIRE sources. We have selected 2%, 5%, and 4% colour-selected bright SPIRE sources to search for overdensities of DSFGs in 2QZCluster, HS1700, and SSA22. We plot the expected colours for Arp 220 as a function of redshifts (Polletta et al. 2007) for comparison. We plot open circles on track of Arp220 every $z = 0.5$ from $z = 0$ to $z = 5.5$.

3.2 SPIRE COLOUR SELECTION

In order to search for DSFGs possibly associated with the protoclusters, we applied a colour constraint to the SPIRE detected sources. The S_{350}/S_{250} and S_{500}/S_{350} colours were used to select the sources with single grey body SEDs at the protocluster's redshift ranges, with dust temperatures of $T_d = 30 - 40$ K, and a dust emissivity $\beta = 1.5$. Casey et al. (2012) measured the dust temperatures of SPIRE-selected DSFGs and showed that they are in the range of $T_d = 20 - 60$ K. The dust emissivity index is determined by Hildebrand (1983), and typically $\beta = 1.0 - 2.0$ for DSFGs. Different values of β do not significantly affect our conclusion, yielding almost the same temperature and SPIRE colours. We included flux errors of ± 20% in estimating the uncertainties in the SPIRE colours. Figure 2 shows S_{500}/S_{350} vs. S_{350}/S_{250} colour-colour diagram of the SPIRE sources in the three protoclusters.

We derived $L_{\rm FIR}$ (8 − 1000 μm) by fitting single grey body SEDs with T_d a free parameter. From the sources selected based on the SPIRE colours, we further applied a FIR luminosity cut of $L_{\rm FIR} \geq 5.0 \times 10^{12}$ $L_\odot$ for conservative searching for DSFGs. Thus the lowest flux densities in our samples are (36.0, 30.0, 19.4) mJy for 2QZCluster, (28.8, 26.3, 15.2) mJy for HS1700, and (15.6, 19.2, 12.9) mJy for SSA22 in the SPIRE bands (250, 350, 500) μm, respectively. We finally obtained a sample of colour-selected bright SPIRE sources with colours consistent with the protocluster redshifts by rejecting ∼ 95% of the 250 μm sources (thus we select just 12/643 (2%), 26/579 (5%), and 55/1253 (4%) colour-selected bright SPIRE sources in 2QZCluster,

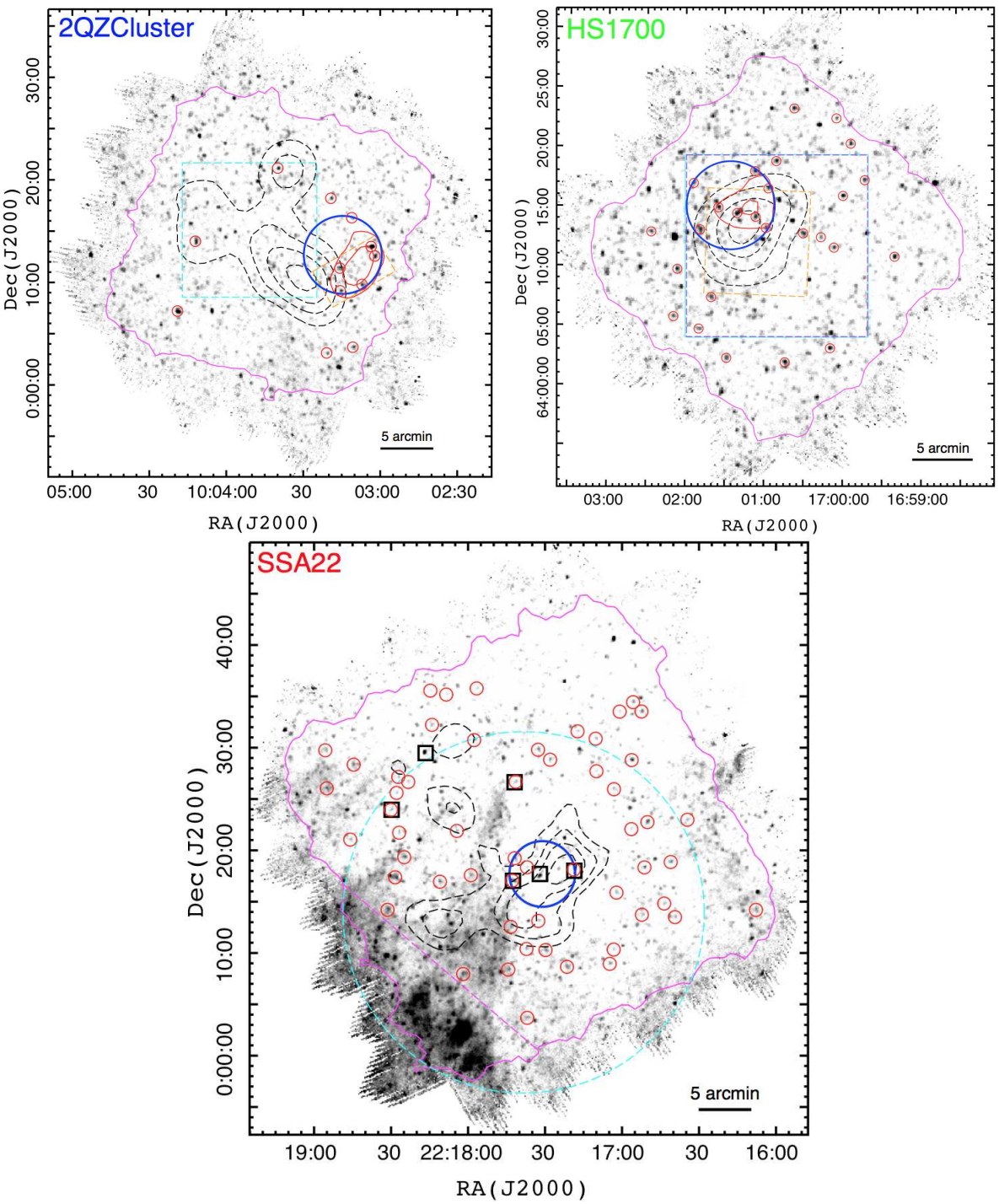

Figure 3. Sky distributions of colour-selected bright 250 μm sources (red circles) over-plotted on the SPIRE 250 μm maps. The areas outlined with magenta contour corresponds to the 30% depth coverage. For SSA22, we do not use below the dashed magenta line due to the high background fluxes. The dashed black contours show the density of 19 HAEs and 3 QSOs (Matsuda et al. 2011) for the 2QZCluster, 45 LBGs for HS1700 (Rudie et al. 2012; Steidel et al. 2014), and 742 LAEs for SSA22 (Yamada et al. 2012) respectively. The steps show 1–4σ, 1–4σ, and 3–6σ for 2QZCluster, HS1700, and SSA22 (smoothed with a Gaussian kernel with a FWHM of 6 comoving Mpc). The red contours show 3–4σ, 4–5σ for colour-selected bright SPIRE sources in 2QZCluster and HS1700 with a same Gaussian kernel (1σ is standard deviation of surface density of colour-selected bright SPIRE sources measured in COSMOS field). The large blue circles show the overdensity of colour-selected bright 250 μm sources for 2QZCluster and HS1700, and colour-selected bright 500 μm sources for SSA22 using filtering a radius of 6 comoving Mpc. We find a 4σ and 5σ overdensity in the 2QZCluster and HS1700 fields. We do not find any significant overdensities of 250 μm sources in SSA22, but we found six colour-selected bright 500 μm sources (black squares), and three sources are concentrated 3′ (∼1.4 Mpc) east to the LAEs overdensity. The dashed cyan and orange boxes in 2QZCluster show the UKIRT/WFCAM (for HAEs) and Subaru/MOIRCS (for HAEs) coverage. The solid cyan, dashed purple, and orange boxes in HS1700 show the Keck/LRIS (for LAEs and LBGs, respectively) and Palomar/WIRC (for HAEs) coverage. The dashed cyan large circle in SSA22 shows ASTE/AzTEC coverage.

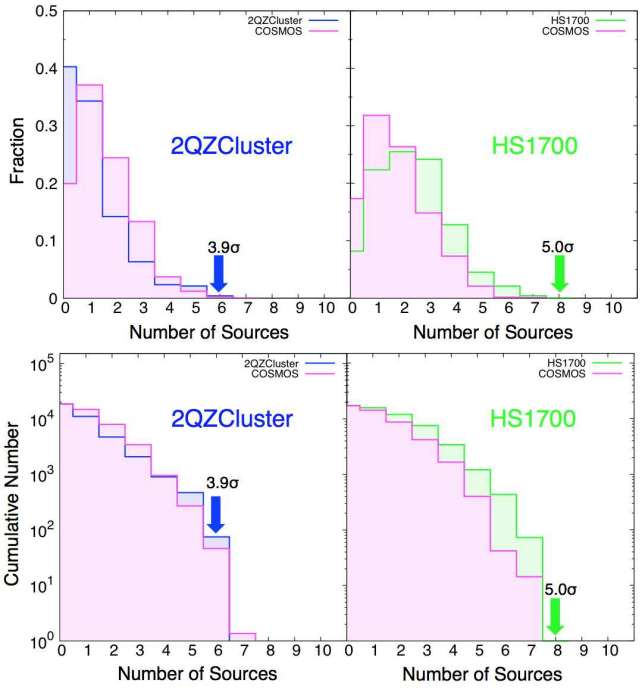

Figure 4. (*Upper*). The density distributions of the colour-selected bright SPIRE sources in 2QZCluster (left) and HS1700 (right) within an aperture radius of 6 comoving Mpc. 2QZCluster tends to have lower number of colour-selected bright SPIRE sources compared with COSMOS field. This could be explained if there are void-like structures within the survey area although there are also overdense regions. In contrast, HS1700 tends to have higher number of sources. (*Lower*). Cumulative number of the apertures with a radius of 6 comoving Mpc. We normalized the cumulative number of COSMOS field to the protoclusters.

HS1700 and SSA22). For COSMOS field, we applied the same colour selection as the three protoclusters to obtain a control sample of field galaxies. We have selected 111/4923 (2%), 140/4923 (3%), and 262/4923 (5%) colour-selected bright SPIRE sources in COSMOS field for 2QZCluster, HS1700, and SSA22 (see also Table 2).

4 RESULTS

4.1 SEARCH FOR OVERDENSITIES

We searched for overdensities in an aperture with a radius of 6 comoving Mpc (3.8′, 3.7′, and 3.2′ radius for $z = 2.2, 2.3$, and 3.1, respectively). This scale corresponds to physical scale of $\sim 1.5-2$ Mpc radius for each protocluster redshift, matching the size of the overdensity of DSFGs around radio galaxies (e.g., Rigby et al. 2014; Dannerbauer et al. 2014). We put down a grid of these apertures every 10″ for the protoclusters and COSMOS field, and counted the number of colour-selected bright SPIRE sources ($L_{\rm FIR} \geq 5.0\times10^{12}\ L_{\odot}$) within each aperture. For SSA22, we excluded a high background region (see in Figure 3).

We found 3.9σ and 5.0σ overdensities in the 2QZCluster and HS1700 fields respectively, but did not find any significant ($> 3\sigma$) overdensities in the SSA22 field. We calculated the significance of overdensity, $\sigma_{\rm pc} = (n_{\rm pc}-n_{\rm ave})/\sigma_{\rm ave}$, where $n_{\rm pc}$ is the number of colour-selected bright SPIRE sources in overdense region (6 comoving Mpc search radius) of the protocluster fields, $n_{\rm ave}$ is the average number within a 6 comoving Mpc search radius for COSMOS field, and $\sigma_{\rm ave}$ is the standard deviation of $n_{\rm ave}$. We also searched for overdensities of colour-selected bright SPIRE sources in case for 10% and 30% flux error boundaries in Figure 2. The result does not significantly change for 20% and 30% boundaries. We found 30% boundary shows same position of overdensities of colour-selected bright SPIRE sources compared with that of 20% boundary in 2QZCluster and HS1700. We found 10% boundary is not suitable because the number of colour-selected bright SPIRE sources are too small to search for overdensities. In Figure 3, we show the sky distribution of the colour-selected bright SPIRE sources. We also show the density of 19 HAEs and 3 QSOs (Matsuda et al. 2011) for 2QZCluster, 45 LBGs for HS1700 (Rudie et al. 2012; Steidel et al. 2014), and 742 LAEs for SSA22 (Yamada et al. 2012) respectively.

We searched for overdensities of the colour-selected bright SPIRE sources in the COSMOS field in an identical manner as for the protocluster fields. We plot the density distribution of the colour-selected bright SPIRE sources for the 2QZCluster, HS1700 and COSMOS fields in Figure 4. The histogram shows the distribution of the number of colour-selected bright SPIRE sources within a 6 comoving Mpc aperture (normalized by the number of searched apertures). We found that 2QZCluster hasa low number of sources. The fraction of the apertures which have no sources is about two times higher compared with COSMOS field. This suggests that there is a void like distribution while there are also overdensities in 2QZCluster. In contrast, HS1700 tends to have larger number of colour-selected bright SPIRE sources in the search apertures.

We also plot the cumulative number of the cricles in Figure 4. We normalized the cumulative number of COSMOS field to the protoclusters. We found that the normalized cumulative number with $> 3.9\sigma$ overdensities in 2QZCluster field is about two times higher than that in the COSMOS field. There are no overdensities in the COSMOS field which contain eight colour-selected bright SPIRE sources (5.0σ) as HS1700. This means that such overdensities are preferentially located in the protoclusters.

4.2 2QZCLUSTER

In the 2QZCluster field, an overdensity of colour-selected bright SPIRE sources were found 4.5′ (∼2.2 Mpc) west to the HAEs overdensity.

We searched for the counterparts of SPIRE sources with HAEs and QSOs in 2QZCluster, which are summarized by Matsuda et al. (2011), although the SPIRE overdense region did not have Hα image with UKIRT/WFCAM (see Figure 3). In total, 19 HAEs and 3 QSOs are within the 174 arcmin^2 overlap region. We define the following quality criteria based on Downes et al. (1986) for assessing the robustness of identified candidate counterparts. We classify sources with $p \leq 0.05$ as secure counterparts, and those with $0.05 < p \leq 0.10$ as tentative counterparts. We calculated the p-value defined by $p = 1-\exp(-\pi {\rm n}\theta^2)$ where n is the source density, θ is the angular offset. We searched for counterparts within 11″ radius from the centre of the SPIRE sources. This

search radius corresponds to ∼40% beam response in 250 μm band.

For the QSOs, 1 optically luminous QSO, which is known as 2QZC-C1-HAE2 (Matsuda et al. 2011), coincides with one of our colour-selected bright SPIRE source 2QZCluster-SPIRE10 (2.7″ offset). The p-value is lower than 0.01, suggesting a secure counterpart, the probability of chance association of counterparts is lower than 1%. 2QZ-C1-HAE3 also coincides with our SPIRE source 2QZCluster-SPIRE124 (5.6″ offset) as a secure counterpart. Such optically luminous FIR bright QSOs are thought to be in a transient phase between DSFGs and QSOs (Simpson et al. 2012). No other HAEs matched with colour-selected bright SPIRE sources. We then repeated this matching using all 250 μm sources, and found five secure HAE counterparts (see Table 11).

We recently conducted Subaru/MOIRCS follow-up NB imaging observations in May 5, 2015 to search for new HAEs as well as counterparts of the SPIRE sources in the SPIRE overdense region ($4' \times 7'$; dashed orange box in Figure 3). The total exposure time of K_s and NB data is each 1.5 and 2.4 ksec, respectively. The 5σ detection limit of NB $<$ 19.8 (Vega) is almost the same as the previous HAE search depth (NB $<$ 19.9 in Vega) by Matsuda et al. (2011).

We find no new HAE within the area. This may suggest that the area is actually a little under-dense in terms of bright HAE, because Matsuda et al. (2011) claim an average field count of 0.09 per arcmin^2, which corresponds to two or three HAEs per MOIRCS FOV. Such void structures adjacent to protocluster has been reported previously (e,g., Koyama et al. 2013; Saito et al. 2015).

4.3 HS1700

In HS1700, the overdensity peak of colour-selected bright SPIRE sources coincides with that of the protocluster member galaxies (2.1′ offset, corresponding to ∼ 1.0 Mpc).

We searched for the counterparts of SPIRE sources using UV-selected (BX/BM) star-forming galaxies (LBGs), HAEs, LAEs, and DRGs in the SPIRE overdense region. There are 3010 LBGs within 256 arcmin^2, 123 LAEs are within 219 arcmin^2, 83 HAEs and 75 DRGs are within 72 arcmin^2. The LBG catalogues are from the KBSS (Keck Baryonic Structure Survey; Rudie et al. 2012; Steidel et al. 2014). HS1700 is one of the fifteen QSO fields intensively studied in KBSS. The Hα and Lyα NB catalogues are from Milan BogosavljevićâĂŹs Ph.D thesis (Bogosavljević 2010). Individual properties of LBGs, LAEs and observations are described in Shapley et al. (2005), Erb, Bogosavljević, & Steidel (2011), Kulas et al. (2013), and Erb et al. (2014). In addition, for the Hα narrow band imaging, we used the Brγ filter (Palomar WIRC, center wavelength 2.17 μm, FWHM=297 Å). The narrow band selection criteria are NB $<$ 20.5 (Vega) and NB $-K_s \leq -0.75$. The DRGs have selected with $J - K > 2.3$ to a limit of $K_s = 21$ (Vega). We define the quality criteria, and classify sources with p-value described above. We deduced the number density of 45 LBGs which have spectroscopically confirmed redshift in the protocluster (i.e., in the overdensity of $z = 2.285 - 2.315$) separately from remaining 2965 LBGs outside of overdensity. We searched for counterparts within 11″ radius from the centre of the SPIRE sources.

We found three colour-selected bright SPIRE sources that have secure counterparts (see Table 12). But one of the LAEs BNB1, the spectrum of this object is extremely odd and that makes difficult to identify the redshift. We identified it as a âĂIJLo-BALâĂİ QSO and it is more likely to have $z \sim 2.00$, so we do not treat as it is a protocluster member galaxy.

We also found one LAE and LBG are secure, and one DRG and LAE are tentative counterparts of colour-selected faint (i.e., $L_{\rm FIR} < 5.0 \times 10^{12}\ L_\odot$) SPIRE source. For the SPIRE sources which are not selected with our colour selection, but have at least one SPIRE band above 12 mJy, we found two secure LAEs, three secure HAEs, and one tentative HAE. Thus, we conclude that seven SPIRE sources in the overdensity have secure counterparts of protocluster galaxies (see Table 12).

In order to assess the success rate of the SPIRE colour selection, we compared the matching result for colour-selected bright/faint SPIRE sources and all 250 μm sources lying within overdensity. We assumed that all HAEs and LAEs are associated with the protocluster except for BNB1, although we should note that the HAEs without spectroscopic follow-up are much less likely than spectroscopic confirmed HAEs to be at the cluster redshift. For all secure counterparts, the fractions are 2/7(29%), 1/5(20%), and 4/28(14%), respectively. This suggests that our SPIRE colour selection can select possible protocluster members with three times higher probability compared to not colour-selected sources.

In the HS1700 field, there are several foreground galaxy groups in the field. A $z = 0.453$ group is very close to the position of HS1700-SPIRE24. Indeed, Peter et al. (2007) found that BX913 is lensed by the group. We calculated a magnification factor by using GLAFIC (Oguri 2010). We used a halo mass of $M/h = 1 \times 10^{14}\ M_\odot$ (Israel et al. 2014) and a concentration parameter of c=6 (Bhattacharya et al. 2013). We found that the second nearest (1.5′ away from group center) SPIRE source is affected only ∼5% magnification, so we conclude that only the HS1700-SPIRE24 could be affected by lensing.

4.4 SSA22

The maximum number of colour-selected bright SPIRE sources found in on 6 comoving Mpc aperture was five, corresponding to a 1.6σ overdensity. This suggests that SSA22 does not have any significant overdensities of colour-selected bright 250 μm sources. But, this could be a problem for SSA22 at $z = 3.1$ because DSFGs would start to drop out at 250 μm. Here we searched for an overdensity of colour-selected bright 500 μm detected sources with identical colour selection and luminosity cut in §3.2. We found six colour-selected bright 500 μm sources in the SSA22 field, and three sources are concentrated 3′ (∼1.4 Mpc) east to the LAEs overdensity (Figure 3). For 350 μm sources, we did not find any significant overdensities as same as 250 μm sources.

We investigated AzTEC 1.1 mm counterparts in Umehata et al. (2014, 2015) for the five colour-selected bright 500 μm sources within ∼800 arcmin^2 overlapped region (Figure 3). We searched for the counterparts within a radius of 14″ (half of AzTEC 1.1 mm FWHM). We found that four colour-selected bright 500 μm sources have

been matched (SSA22-AzTEC1, 2, 5, and 34). Thus $\sim 80\%$ colour-selected bright 500 μm sources are matched with AzTEC 1.1 mm sources.

5 DISCUSSION & SUMMARY

We searched for DSFGs associated with three protoclusters at $z = 2-3$ (2QZCluster, HS1700, SSA22) using *Herschel*/SPIRE. In the 2QZCluster and HS1700 field, we found 4σ and 5σ overdensities of the colour-selected bright SPIRE sources on a scale of 6 comoving Mpc. In the SSA22, we did not find any significant overdensities of 250 μm sources, but we found that three colour-selected bright 500 μm sources are concentrated on a scale of 6 comoving Mpc. The results suggest possible activity associated with enhanced dusty star-formation in protoclusters at $z \sim 2-3$.

We derive the star-formation rate (SFR) density of 2QZCluster, HS1700 and SSA22 to compare with the average value of the Universe. The SFR of DSFGs is often converted from far-infrared luminosity, although the conversion from $L_{\rm FIR}$ to SFR is not straightforward and relies on the dust composition and initial mass function (IMF). Most works on DSFGs assume the conversion given by SFR ($M_\odot$ yr^{-1}) = 4.5×10^{-44} $L_{\rm FIR}$ (erg s^{-1}) or 1.7×10^{-10} $L_{\rm FIR}$ ($L_\odot$) (Kennicutt 1998), where $L_{\rm FIR}$ is the integrated luminosity of $8-1000$ μm. This conversion takes the radiative transfer models of Leitherer & Heckman (1995) and a Salpeter IMF (Salpeter 1955).

We used a simple estimation to calculate the integrated SFR densities by assuming that all colour-selected bright SPIRE sources in the overdensities are associated with protoclusters. In addition, we also included sources with S/N > 2 in all three SPIRE bands within a radius of 1 Mpc (physical) following Clements et al. (2014) analysis of *Planck* clumps with *Herschel*/SPIRE. Because this radius of 1 Mpc circles are smaller than our search radius (6 comoving Mpc, $\sim 1.5-2$ Mpc in physical), we adjusted the position of the smaller aperture to contain as many colour-selected bright SPIRE sources as possible. This enables us to select regions similar to *Planck* clumps in Clements et al. (2014). The 1σ instrumental noise of Clements's work ranges from $2.5-2.8$ mJy at 250 μm, $2.1-2.3$ mJy at 350 μm and $3.0-3.3$ mJy at 500 μm (Clements et al. 2014), which is similar to our survey. For all SPIRE sources within a 1 Mpc radius, we fitted single grey body SEDs with fixed $T_d = 35$ K, $\beta = 1.5$ and the protocluster's redshifts, and derived $L_{\rm FIR}$. We excluded one colour-selected bright SPIRE source HS1700-SPIRE30 from this discussion because it is very close to $z = 0.08$ SDSS galaxy, and its *Spitzer*/MIPS 24 μm flux density is very high (~ 200 μJy). We found that Mips 24 μm flux densities of other colour-selected bright SPIRE sources in HS1700 are consistent with that of typical high-z star-forming galaxies. 2QZCluster does not have any *Spitzer* images.

Figure 5 shows our results and compare to previous studies in the literature. We calculated SFR with Bell (2003)'s $L_{\rm FIR}$ correction to follow Clements et al. (2014) analysis. The derived SFR densities are 10^3–10^4 times higher than the global SFR density seen in Madau & Dickinson (2014). This comparison indicates enhanced star-formation activities in protoclusters at $z \sim 2-3$. The enhancement of dusty star-formation activity within our protoclusters is consistent with that seen for *Planck* clumps (Clements et al. 2014). Dannerbauer et al. (2014) presents results based on APEX/LABOCA 870 μm observations around MRC1138−262 at $z = 2.16$, showing that at least six DSFGs are likely part of the protocluster. The SFR density ~ 1500 $M_\odot$ yr^{-1} Mpc^{-3} is similar to Clements et al. (2014) and our protoclusters study. We also plot the error bars in Figure 5. The high end shows the case when including all sources in 1 Mpc radius and the low end shows the case for subtracting field average values. We deduced field values by calculating average number of sources and average luminosity in 1 Mpc radius apertures in the COSMOS field.

Table 3. Estimated SFR and assumed volume for Figure 5.

Field	z	SFR^a ($M_\odot$ yr^{-1})	r^b (Mpc)	V^c (Mpc^3)	SFR$_{\rm min}{}^d$ ($M_\odot$ yr^{-1})
All sources					
2QZCluster	2.230 ± 0.016	5000	1.0	4.2	150
HS1700	2.300 ± 0.015	4500	1.0	4.2	280
SSA22	3.09 ± 0.03	7500	1.0	4.2	310
Field corrected values					
2QZCluster	2.230 ± 0.016	1000	1.0	4.2	-
HS1700	2.300 ± 0.015	2000	1.0	4.2	-
SSA22	3.09 ± 0.03	4700	1.0	4.2	-

Notes. (a): Integrated SFR derived from SPIRE sources which are included in column 4 radius. (b) − (c): Used radius and volume to calculate SFR density. (d): Minimum SFR of SPIRE source which is included in integrated SFR.

In Table 3, we summarized the estimated SFR and assumed volume plotted in Figure 5. We also caluculated SFR density in an aperture using a radius of 6 comoving Mpc in the same manner. These radii are 1.9, 1.8 and 1.5 Mpc in physical units for 2QZCluster, HS1700 and SSA22, respectively, and the results do not change compared to the case of 1 Mpc.

What causes the enhanced dusty star-forming activity in our protoclusters? One possible answer to this is galaxies mergers. For instance, Casey et al. (2015) investigated the morphology of the galaxies in a protocluster to search for interaction/merger state by using *HST* H-band imaging data. Although the sample size is limited, they found that the fraction of irregular and interacting galaxies among the LBGs and DSFGs is 1.5 times higher in the protocluster than in the field. Webb et al. (2015) suggested that dusty star formation at the center of a $z = 1.7$ cluster is being driven by galaxy-galaxy interaction, involving a far-infrared luminous Bright Cluster Galaxy (BCG). Because there are strong correlation between the major-merger and the far-infrared luminosity (Kartaltepe et al. 2010, 2012; Engel et al. 2010; Hung et al. 2013), higher major mergers rate in protoclusters could induce dusty star-formation. N-body simulation also predicts that progenitors of cluster and group haloes at $z > 2$ have $3-5\times$ higher major merger rates than isolated halos (Gottlöber, Klypin, & Kravtsov 2001). The facts that the colour-selected bright SPIRE sources are significantly concentrated in HS1700 and 2QZCluster would support such simultaneously major merging phenomenon. However, further observations are needed to investigate the processes of dusty star-forming activity in these protoclusters.

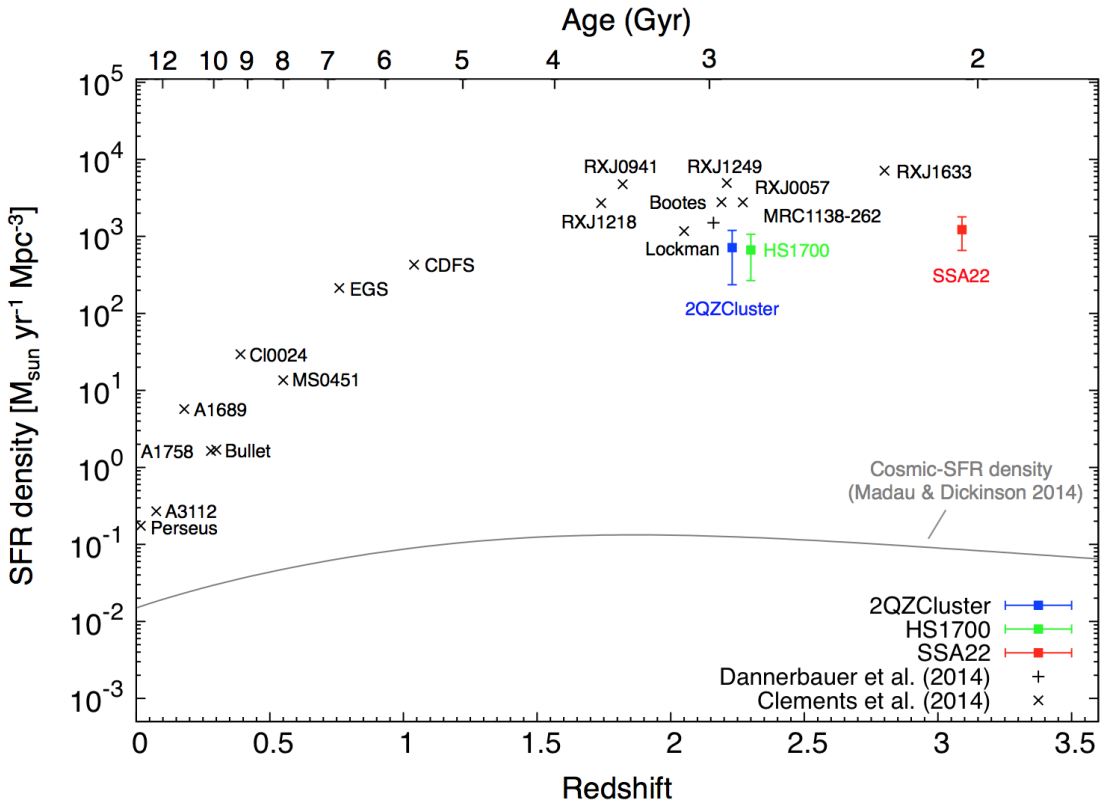

Figure 5. SFR density of clusters, protoclusters and global cosmic SFR densities. The SFR densities of our protoclusters are 10^3–10^4 times higher than the global SFR density (Madau & Dickinson 2014). We show the compilation from Dannerbauer et al. (2014) and data from Clements et al. (2014), which original literature are following; *IRAS* measurements of Perseus from Meusinger, Brunzendorf, & Krieg (2000), BLAST measurements of A3112 from Braglia et al. (2011), *ISO* measurements of A1689 from Fadda et al. (2000), and *Spitzer* measurements of A1758 from Haines et al. (2009), Bullet cluster from Chung et al. (2010), Cl0024+16 and MS0451-03 from Geach et al. (2006). RXJ0057, RXJ0941, RXJ1218, RXJ1249 and RXJ1633 are based on JCMT/SCUBA from Stevens et al. (2010).

ACKNOWLEDGMENTS

We thank the anonymous referee for helpful comments which significantly improved the clarity of this paper. We thank Scott Chapman, James Colbert, Emanuele Daddi, Koichiro Nakanishi and Kazuhiro Shimasaku for useful discussions and supports. Rhythm Shimakawa and Mariko Kubo made enormous contribution to analyses. We acknowledge Masaru Kajisawa for our use of his MOIRCS fringe-removal software (Kajisawa et al. 2015) during the data reduction.

Herschel is an ESA space observatory with science instruments provided by European-led Principal Investigator consortia and with important participation from NASA. SPIRE has been developed by a consortium of institutes led by Cardiff University (UK). Subaru Telescope, which is operated by the National Astronomical Observatory of Japan. UKIRT is funded by the STFC (UK). The W.M. Keck Observatory was made possible by the generous financial support of the W.M. Keck Foundation. The authors wish to recognize and acknowledge the very significant cultural role and reverence that the summit of Mauna Kea has always had within the indigenous Hawaiian community. We are most fortunate to have the opportunity to conduct observations from this mountain.

This research was supported in part by a grant from the Hayakawa Satio Fund awarded by the Astronomical Society of Japan. YM acknowledges support from JSPS KAKENHI Grant Number 20647268. IRS acknowledges support from STFC (ST/L00075X/1), the ERC Advanced Grant DUSTYGAL (321334) and a Royal Society/Wolfson Merit Award. BH acknowledges support from JSPS KAKENHI Grant Number 15K17616. HU acknowledges support from Grant-in-Aid for JSPS Fellows, 26.11481.

REFERENCES

Bai L., et al., 2007, ApJ, 664, 181
Bell E. F., 2003, ApJ, 586, 794
Béthermin M., et al., 2012, A&A, 542, AA58
Bhattacharya S., Habib S., Heitmann K., Vikhlinin A., 2013, ApJ, 766, 32
Braglia F. G., et al., 2011, MNRAS, 412, 1187
Brodwin M., et al., 2013, ApJ, 779, 138
Bogosavljević M., 2010, PhDT,
Casey C. M., et al., 2012, ApJ, 761, 140
Casey C. M., et al., 2015, ApJ, 808, L33
Casey C. M., 2016, arXiv, arXiv:1603.04437
Chapman S. C., et al., 2015, MNRAS, 449, L68
Chung S. M., Gonzalez A. H., Clowe D., Markevitch M., Zaritsky D., 2010, ApJ, 725, 1536
Clements D. L., et al., 2014, MNRAS, 439, 1193
Croom S. M., Smith R. J., Boyle B. J., Shanks T., Loaring N. S., Miller L., Lewis I. J., 2001, MNRAS, 322, L29

Croom S. M., Smith R. J., Boyle B. J., Shanks T., Miller L., Outram P. J., Loaring N. S., 2004, MNRAS, 349, 1397
Dannerbauer H., et al., 2014, A&A, 570, AA55
Digby-North J. A., et al., 2010, MNRAS, 407, 846
Downes A. J. B., Peacock J. A., Savage A., Carrie D. R., 1986, MNRAS, 218, 31
Elbaz D., et al., 2007, A&A, 468, 33
Ellis R. S., Smail I., Dressler A., Couch W. J., Oemler A., Jr., Butcher H., Sharples R. M., 1997, ApJ, 483, 582
Engel H., et al., 2010, ApJ, 724, 233
Erb D. K., Bogosavljević M., Steidel C. C., 2011, ApJ, 740, L31
Erb D. K., et al., 2014, ApJ, 795, 33
Fadda D., Elbaz D., Duc P.-A., Flores H., Franceschini A., Cesarsky C. J., Moorwood A. F. M., 2000, A&A, 361, 827
Geach J. E., et al., 2006, ApJ, 649, 661
Gottlöber S., Klypin A., Kravtsov A. V., 2001, ApJ, 546, 223
Granato G. L., Ragone-Figueroa C., Domínguez-Tenreiro R., Obreja A., Borgani S., De Lucia G., Murante G., 2015, MNRAS, 450, 1320
Griffin M. J., et al., 2010, A&A, 518, L3
Haines C. P., Smith G. P., Egami E., Okabe N., Takada M., Ellis R. S., Moran S. M., Umetsu K., 2009, MNRAS, 396, 1297
Hayashino T., et al., 2004, AJ, 128, 2073
Hildebrand R. H., 1983, QJRAS, 24, 267
Hung C.-L., et al., 2013, ApJ, 778, 129
Israel H., Reiprich T. H., Erben T., Massey R. J., Sarazin C. L., Schneider P., Vikhlinin A., 2014, A&A, 564, A129
Ivison R. J., Dunlop J. S., Smail I., Dey A., Liu M. C., Graham J. R., 2000, ApJ, 542, 27
Ivison R. J., et al., 2013, ApJ, 772, 137
Kajisawa M., Morishita T., Taniguchi Y., Kobayashi M. A. R., Ichikawa T., Fukui Y., 2015, ApJ, 801, 134
Kartaltepe J. S., et al., 2010, ApJ, 721, 98
Kartaltepe J. S., et al., 2012, ApJ, 757, 23
Kennicutt R. C., Jr., 1998, ARA&A, 36, 189
Koyama Y., Kodama T., Tadaki K.-i., Hayashi M., Tanaka M., Smail I., Tanaka I., Kurk J., 2013, MNRAS, 428, 1551
Kulas K. R., et al., 2013, ApJ, 774, 130
Lehmer B. D., et al., 2009, ApJ, 691, 687
Lehmer B. D., et al., 2009, MNRAS, 400, 299
Lehmer B. D., et al., 2013, ApJ, 765, 87
Leitherer C., Heckman T. M., 1995, ApJS, 96, 9
Lilly S., et al., 1998, ApJ, 500, 75
Lutz D., et al., 2001, A&A, 378, 70
Ma C.-J., et al., 2015, ApJ, 806, 257
Madau P., Dickinson M., 2014, ARA&A, 52, 415
Matsuda Y., et al., 2004, AJ, 128, 569
Matsuda Y., et al., 2011, MNRAS, 416, 2041
Meusinger H., Brunzendorf J., Krieg R., 2000, A&A, 363, 933
Nguyen H. T., et al., 2010, A&A, 518, LL5
Oguri M., 2010, PASJ, 62, 1017
Oliver S. J., et al., 2012, MNRAS, 424, 1614
Ott S., 2010, ASPC, 434, 139
Peter A. H. G., Shapley A. E., Law D. R., Steidel C. C., Erb D. K., Reddy N. A., Pettini M., 2007, ApJ, 668, 23
Pilbratt G. L., et al., 2010, A&A, 518, L1
Polletta M., et al., 2007, ApJ, 663, 81
Rigby E. E., et al., 2014, MNRAS, 437, 1882
Rudie G. C., et al., 2012, ApJ, 750, 67
Saito T., et al., 2015, MNRAS, 447, 3069
Salpeter E. E., 1955, ApJ, 121, 161
Shapley A. E., Steidel C. C., Erb D. K., Reddy N. A., Adelberger K. L., Pettini M., Barmby P., Huang J., 2005, ApJ, 626, 698
Simpson J. M., et al., 2012, MNRAS, 426, 3201
Smail I., Ivison R. J., Blain A. W., Kneib J.-P., 1998, ApJ, 507, L21
Smail I., et al., 2014, ApJ, 782, 19
Smith A. J., et al., 2012, MNRAS, 419, 377
Steidel C. C., Adelberger K. L., Dickinson M., Giavalisco M., Pettini M., Kellogg M., 1998, ApJ, 492, 428
Steidel C. C., Adelberger K. L., Shapley A. E., Pettini M., Dickinson M., Giavalisco M., 2000, ApJ, 532, 170
Steidel C. C., Adelberger K. L., Shapley A. E., Erb D. K., Reddy N. A., Pettini M., 2005, ApJ, 626, 44
Steidel C. C., et al., 2014, ApJ, 795, 165
Stevens J. A., et al., 2003, Natur, 425, 264
Stevens J. A., Jarvis M. J., Coppin K. E. K., Page M. J., Greve T. R., Carrera F. J., Ivison R. J., 2010, MNRAS, 405, 2623
Swinyard B. M., et al., 2010, A&A, 518, L4
Tamura Y., et al., 2009, Natur, 459, 61
Tran K.-V. H., et al., 2010, ApJ, 719, L126
Umehata H., et al., 2014, MNRAS, 440, 3462
Umehata H., et al., 2015, ApJ, 815, L8
Valtchanov I., et al., 2013, MNRAS, 436, 2505
Webb T., et al., 2015, ApJ, 809, 173
Wylezalek D., et al., 2013, MNRAS, 428, 3206
Yamada T., Nakamura Y., Matsuda Y., Hayashino T., Yamauchi R., Morimoto N., Kousai K., Umemura M., 2012, AJ, 143, 79

Table 4. Number of sources which have fluxes above 12 mJy in each bands.

	COSMOS	SSA22	HS1700	2QZCluster
250 μm	2552	699	356	365
350 μm	1944	529	259	260
500 μm	961	252	133	116

Table 5. Number counts at 250 μm. The errors take into account the statistical uncertainties, including the Poisson noise.

Central flux (mJy)	Flux bin (mJy)	Number counts (dN/dS) [mJy^{-1} deg^{-2}] SSA22	HS1700	2QZCluster	COSMOS
16.8	12.0 – 21.6	148.1 ± 7.2	137.2 ± 10.2	157.1 ± 10.7	158.1 ± 4.2
23.8	21.6 – 26.0	70.0 ± 7.3	92.1 ± 12.3	73.0 ± 10.8	87.5 ± 4.6
33.6	26.0 – 41.2	31.5 ± 2.6	37.6 ± 4.2	34.0 ± 4.0	36.4 ± 1.6
47.4	41.2 – 53.6	6.5 ± 1.3	11.7 ± 2.6	7.9 ± 2.1	10.4 ± 0.9
67.0	53.6 – 80.4	1.6 ± 0.5	4.0 ± 1.0	2.3 ± 0.8	2.7 ± 0.3
94.6	80.4 – 108.8	0.12 ± 0.12	0.51 ± 0.36	0.74 ± 0.43	0.74 ± 0.17
133.7	108.8 – 158.6	0.07 ± 0.07	0.15 ± 0.15	0.42 ± 0.24	0.06 ± 0.04
188.8	158.6 – 219.0	-	-	-	-

Table 6. Number counts at 350 μm. The errors take into account the statistical uncertainties, including the Poisson noise.

Central flux (mJy)	Flux bin (mJy)	Number counts (dN/dS) [mJy^{-1} deg^{-2}] SSA22	HS1700	2QZCluster	COSMOS
16.8	12.0 – 21.6	113.6 ± 6.3	107.0 ± 9.0	116.4 ± 9.2	127.4 ± 3.7
23.8	21.6 – 26.0	60.1 ± 6.8	69.1 ± 10.7	68.3 ± 10.4	62.2 ± 3.9
33.6	26.0 – 41.2	23.1 ± 2.3	23.8 ± 3.4	18.8 ± 2.9	28.5 ± 1.4
47.4	41.2 – 53.6	3.2 ± 0.9	8.8 ± 2.3	3.4 ± 1.4	5.9 ± 0.7
67.0	53.6 – 80.4	0.9 ± 0.3	2.4 ± 0.8	2.3 ± 0.8	1.5 ± 0.2
94.6	80.4 – 108.8	-	-	-	0.04 ± 0.04
133.7	108.8 – 158.6	-	-	0.14 ± 0.14	-
188.8	158.6 – 219.0	-	-	-	-

Table 7. Number counts at 500 μm. The errors take into account the statistical uncertainties, including the Poisson noise.

Central flux (mJy)	Flux bin (mJy)	Number counts (dN/dS) [mJy^{-1} deg^{-2}] SSA22	HS1700	2QZCluster	COSMOS
16.8	12.0 – 21.6	68.3 ± 4.9	70.8 ± 7.3	53.1 ± 6.2	75.2 ± 2.9
23.8	21.6 – 26.0	23.6 ± 4.2	21.4 ± 5.9	39.7 ± 7.9	27.3 ± 2.6
33.6	26.0 – 41.2	3.7 ± 0.9	10.0 ± 2.2	6.4 ± 1.7	9.7 ± 0.8
47.4	41.2 – 53.6	1.3 ± 0.6	2.3 ± 1.2	1.7 ± 1.0	1.6 ± 0.4
67.0	53.6 – 80.4	0.1 ± 0.1	0.27 ± 0.27	0.26 ± 0.26	0.08 ± 0.06
94.6	80.4 – 108.8	-	-	-	-
133.7	108.8 – 158.6	-	-	-	-
188.8	158.6 – 219.0	-	-	-	-

Table 8. SPIRE sources catalogue of 2QZCluster. The full table is available online.

ID	R.A. (J2000)	Dec. (J2000)	S_{250} (mJy)	S_{350} (mJy)	S_{500} (mJy)
2QZCluster-SPIRE1	150.81846968368112	0.029424092103377656	127.0 ± 2.1	54.2 ± 1.9	24.6 ± 2.2
2QZCluster-SPIRE2	150.76480950482065	0.22501254698200338	139.1 ± 2.4	117.9 ± 1.8	71.4 ± 2.3
2QZCluster-SPIRE3	150.91517959664077	0.3909833462929028	111.4 ± 2.4	55.2 ± 1.8	21.2 ± 2.4
2QZCluster-SPIRE4	151.02463506680982	0.1206541823404277	97.4 ± 2.2	54.2 ± 1.8	26.5 ± 2.4
2QZCluster-SPIRE5	151.04455762206453	0.4047339937359634	93.6 ± 2.3	61.3 ± 1.8	24.2 ± 2.2
2QZCluster-SPIRE6	151.07930718745527	0.12006911913976963	84.1 ± 2.3	58.9 ± 1.8	31.3 ± 2.3
2QZCluster-SPIRE7	151.11225122198036	0.17674219593981788	66.1 ± 2.2	36.2 ± 2.1	13.2 ± 2.1
2QZCluster-SPIRE8	150.7066091154151	0.2830585502030584	67.4 ± 2.3	54.5 ± 1.8	18.4 ± 2.2
2QZCluster-SPIRE9	150.94968775985714	0.33116978814976	64.4 ± 2.2	22.2 ± 1.9	0.0 ± 2.1
2QZCluster-SPIRE10	150.91631977926835	0.3524558479517708	60.1 ± 2.1	64.7 ± 1.8	45.6 ± 2.0

Table 9. SPIRE sources catalogue of HS1700. The full table is available online.

ID	R.A. (J2000)	Dec. (J2000)	S_{250} (mJy)	S_{350} (mJy)	S_{500} (mJy)
HS1700-SPIRE1	255.53646683056928	64.2060083253161	422.6 ± 3.1	181.4 ± 1.9	67.3 ± 2.4
HS1700-SPIRE2	255.07094202680116	64.36337246187729	112.4 ± 2.2	49.0 ± 1.9	19.5 ± 2.2
HS1700-SPIRE3	255.10511462429938	64.14686204692669	86.2 ± 2.4	51.5 ± 2.0	21.4 ± 2.1
HS1700-SPIRE4	255.15806474143926	64.22916135482777	85.8 ± 2.5	60.5 ± 1.8	27.9 ± 2.2
HS1700-SPIRE5	254.99437853070503	64.26410380634614	70.8 ± 2.1	76.4 ± 1.7	51.2 ± 2.2
HS1700-SPIRE6	254.91863041158092	64.21174308418698	76.7 ± 2.4	44.4 ± 1.7	17.6 ± 2.3
HS1700-SPIRE7	255.22359843297363	64.38646521955137	65.7 ± 2.2	21.3 ± 1.9	13.0 ± 2.3
HS1700-SPIRE8	254.82938021291324	64.17873107989598	68.7 ± 2.3	59.4 ± 1.7	27.6 ± 2.2
HS1700-SPIRE9	255.20168755944053	64.25859055126669	66.3 ± 2.2	35.3 ± 2.1	16.2 ± 2.2
HS1700-SPIRE10	255.1823543841818	64.03153372522755	64.7 ± 2.2	64.8 ± 1.9	31.2 ± 2.1

Table 10. SPIRE sources catalogue of SSA22. The full table is available online.

ID	R.A. (J2000)	Dec (J2000)	S_{250} (mJy)	S_{350} (mJy)	S_{500} (mJy)
SSA22-SPIRE1	334.264444128561	0.6764415586203842	135.3Âś2.2	71.3Âś1.9	30.4Âś2.3
SSA22-SPIRE2	334.57160684240256	0.49219161422544583	93.3Âś2.2	76.7Âś1.7	48.7Âś2.3
SSA22-SPIRE3	334.344178441303	0.3528652232847903	79.2Âś2.2	34.4Âś1.9	10.4Âś2.2
SSA22-SPIRE4	334.34457572927244	0.607307593915126	79.7Âś2.4	56.9Âś1.7	21.9Âś2.0
SSA22-SPIRE5	334.69745115684617	0.3983836901706686	72.9Âś2.2	29.8Âś1.9	12.8Âś2.1
SSA22-SPIRE6	334.392819716858	0.3042332652494624	68.9Âś2.1	33.2Âś1.8	0.0Âś2.1
SSA22-SPIRE7	334.23836274598824	0.40194158606064945	61.8Âś2.1	45.8Âś1.8	8.8Âś2.1
SSA22-SPIRE8	334.55462830631444	0.47701863826781765	62.9Âś2.1	33.3Âś1.8	18.3Âś2.0
SSA22-SPIRE9	334.3848999033597	0.2912395866246295	57.5Âś2.1	49.6Âś1.7	45.7Âś2.2
SSA22-SPIRE10	334.58002216598203	0.35006798763473185	64.3Âś2.3	51.3Âś2.0	30.6Âś2.3

Table 11. Matching results for the SPIRE sources which have HAEs counterparts in 2QZCluster.

ID (SPIRE)	R.A. (J2000)	Dec (J2000)	S_{250} (mJy)	S_{350} (mJy)	S_{500} (mJy)	Counterpart	R.A. (J2000)	Dec (J2000)	Sepa.[a] (arcsec)	p-value[b]	Member[c]
Colour-selected bright SPIRE sources											
2QZCluster-SPIRE10	150.916320	0.352456	60.1 ± 2.1	64.7 ± 1.8	45.6 ± 2.0	QZC-C1-HAE02(QSO)	150.915790	0.353000	2.73	<0.01	Secure
at least one SPIRE band above 12 mJy sources											
2QZCluster-SPIRE124	150.965998	0.249463	21.9 ± 2.2	14.2 ± 1.8	9.7 ± 2.2	QZC-C1-HAE03(QSO)	150.964920	0.250583	5.60	<0.01	Secure
2QZCluster-SPIRE239	151.069470	0.310488	15.4 ± 2.2	4.1 ± 1.8	6.9 ± 2.3	QZC-C1-HAE20	151.069750	0.309167	4.86	<0.01	Secure
2QZCluster-SPIRE251	150.885551	0.168325	15.5 ± 2.2	6.8 ± 2.0	3.7 ± 2.3	QZC-C1-HAE09	150.887370	0.167917	6.71	<0.01	Secure
2QZCluster-SPIRE261	150.852526	0.155903	15.8 ± 2.3	13.8 ± 1.8	12.1 ± 2.2	QZC-C1-HAE05	150.854380	0.155694	6.72	<0.01	Secure
2QZCluster-SPIRE353	150.916183	0.187292	14.4 ± 2.7	12.1 ± 1.8	3.0 ± 2.1	QZC-C1-HAE16	150.915750	0.187722	2.20	<0.01	Secure
2QZCluster-SPIRE372	150.935267	0.238716	10.2 ± 2.2	16.2 ± 1.8	14.0 ± 2.1	QZC-C1-HAE15	150.932670	0.238944	9.39	0.01	Secure

Notes. (a): Separation between SPIRE source and counterparts. (b): p-value based on Downes et al. (1986). (c): We classify sources with $p \leq 0.05$ as secure, and those with $0.05 < p \leq 0.10$ as tentative counterparts.

Table 12. Matching results for the SPIRE sources which have emitter counterparts within overdensity in HS1700.

ID (SPIRE)	R.A. (J2000)	Dec (J2000)	S_{250} (mJy)	S_{350} (mJy)	S_{500} (mJy)	ID (Count.)	R.A. (J2000)	Dec (J2000)	z^a	Sepa.^{b} (arcsec)	p-value^c	Member^d
Colour-selected bright SPIRE sources												
HS1700-SPIRE21	255.3951	64.2484	52.5 ± 2.2	41.2 ± 1.7	21.1 ± 2.2	BNB1	255.3953	64.2479	∼2.00^e	1.63	< 0.01	Secure
						BX980	255.3987	64.2490	-	6.13	0.32	Not
HS1700-SPIRE42	255.2428	64.2196	40.0 ± 2.3	46.4 ± 1.8	34.3 ± 2.1	DRG46	255.2419	64.2195	-	1.37	< 0.01	Secure
						HaNB2	255.2417	64.2196	-	1.75	< 0.01	Secure
HS1700-SPIRE24	255.3349	64.2403	51.5 ± 2.3	63.0 ± 2.0	49.3 ± 2.2	DRG53	255.3378	64.2395	∼ 2.3^f	5.36	0.03	Secure
						HaNB10*	255.3399	64.2384	2.289(abs)	10.43	0.10	Tentative
						BX913*	255.3399	64.2385	2.289(abs), 2.291(neb)	10.29	0.05	Tentative
						BX928	255.3318	64.2405	2.755(Lyα)	4.92	0.22	Not
Colour-selected faint SPIRE sources												
HS1700-SPIRE321	255.2732	64.2046	13.7 ± 2.4	20.2 ± 1.8	15.9 ± 2.1	BNB41*	255.2688	64.2027	2.287(abs)	9.64	0.05	Secure
						MD109*	255.2687	64.2026	2.293(abs,neb)	10.09	0.02	Secure
						DRG38$^+$	255.2669	64.2032	2.286(emi)	10.98	0.10	Tentative
						BNB16$^+$	255.2670	64.2033	2.290(emi)	10.53	0.05	Tentative
at least one SPIRE band above 12 mJy sources												
HS1700-SPIRE70	255.2827	64.2586	31.1 ± 2.2	21.4 ± 1.9	11.0 ± 2.0	BNB155	255.2811	64.2574	2.290(Lyα)	5.13	0.01	Secure
						HaNB27	255.2873	64.2578	-	7.81	0.06	Tentative
HS1700-SPIRE78	255.4358	64.2607	30.3 ± 2.2	16.9 ± 1.7	6.0 ± 2.1	BNB139	255.4331	64.2622	-	6.85	0.02	Secure
HS1700-SPIRE142	255.2668	64.2469	22.7 ± 2.2	12.0 ± 1.8	1.8 ± 2.2	HaNB83	255.2653	64.2487	-	6.67	0.04	Secure
						HaNB76	255.2661	64.2461	-	3.06	0.01	Secure
HS1700-SPIRE179	255.3768	64.1988	19.8 ± 2.2	9.4 ± 1.8	0.5 ± 2.2	HaNB45	255.3796	64.1996	-	5.41	0.03	Secure

Notes. (a): Redshift information of counterparts. (b): Separation between SPIRE source and counterparts. (c): p-value based on Downes et al. (1986). (d): We classify sources with $p \leq 0.05$ as secure, and those with $0.05 < p \leq 0.10$ as tentative counterparts. (e): BNB1 is identified as a âĂIJLo-BALâĂİ QSO and therefore it is difficult to measure redshift. (f): Photometric redshift from Chapman et al. (2015).